

# Description of complex viewing geometries of fusion tomography diagnostics by ray-tracing

M. Carr,<sup>1, a)</sup> A. Meakins,<sup>1</sup> M. Bernert,<sup>2</sup> P. David,<sup>2</sup> C. Giroud,<sup>1</sup> J. Harrison,<sup>1</sup> S. Henderson,<sup>1</sup> B. Lipschultz,<sup>3</sup> F. Reimold,<sup>4</sup> the EUROfusion MST1 Team,<sup>b)</sup> and ASDEX Upgrade team

<sup>1)</sup>CCFE, Culham Science Centre, Abingdon, Oxon, OX14 3DB, UK

<sup>2)</sup>Max-Planck-Institut für Plasmaphysik, 85748 Garching, Germany.

<sup>3)</sup>York Plasma Institute, Department of Physics, University of York, Heslington, York, UK

<sup>4)</sup>Max-Planck-Institut für Plasmaphysik, Greifswald, Germany.

(Dated: 4 June 2018)

Ray-tracing techniques are applied to bolometry, a diagnostic particularly sensitive to machine geometry due to the effect of the finite collection volume subtended by a 3D aperture. Sightlines from the ASDEX Upgrade bolometer foils were ray-traced with a path tracing algorithm, where the optical path is represented by a statistical bundle of ray paths connecting the foil surface with the slit geometry. By using the full 3D machine CAD model for the detector box and first wall, effects such as occlusion and vignetting were included in the calculation of the bolometer's étendue. Inversion matrices calculated with the ray-tracing technique were compared with the more conventional single-ray approach and shown to be naturally more constrained, requiring less regularisation. The two models were tested on a sample radiation scenario and the common single-ray approximation is shown to be insufficient. These results are particularly relevant for the divertor where strong emission gradients may be present. The technique developed generalises well to arbitrarily complex viewing geometries and collimators, opening up a new design space for bolometer configurations that might not normally have been considered.

## I. INTRODUCTION

To protect the divertor components in machines on the scale of ITER and DEMO, a large fraction of the exhaust power entering the scrape of layer must be radiated before it reaches the divertor targets<sup>1</sup>. Multi-channel bolometry is a key diagnostic used in current experiments to facilitate the development of highly radiating divertor scenarios<sup>2</sup>. An accurate bolometric diagnostic is essential for both measuring the total radiated power fraction and determining the spatial distribution of the emissivity.

with  
A bolometer is designed to effectively be a black surface such that it will absorb all photons incident upon it, yielding a measurement of the radiant flux at that surface. Gold is usually used as the absorbing material of choice because it exhibits strong absorption above  $\sim 3\text{eV}$ , which corresponds well to the spectral region where the bulk of the power is radiated in a typical tokamak plasma<sup>2</sup>.

The limited geometric accessibility around tokamak plasmas means most bolometry diagnostics are installed as fans of pinhole cameras at a low number of observation points. The plasma's local emissivity profile is then inferred from the line integrated measurements by means of standard tomography techniques<sup>2,3</sup>. Figure 1 shows

the FLH bolometer camera in situ at ASDEX Upgrade (AUG).

The response of the collimated detectors is often modelled with the line-of-sight approximation, i.e. assuming views along infinitely thin straight lines, which will hereafter be referred to as the single-ray model. However, this approximation is known to be a poor repre with sentation of the detector when the beam width is significantly larger than the inversion grid cell length scale and there are appreciable gradients in the emission profile<sup>4-7</sup>.

The most advanced analytical model was developed by Ingesson et. al.<sup>4</sup> and considers the geometrical response of an ideal rectangular pinhole and detector. The authors also developed a numerical treatment for calculating the response of the as installed JET bolometer detectors which consisted of a rectangular detector with a cylindrical collimator. Occlusion of the detection volume by first wall protection tiles was taken into account through secondary apertures<sup>4</sup>. However this model was not able to take into account the toroidal bending of the voxels due to the nature of the numerical scheme used. Although negligible for JET, this effect has been shown to be significant on other devices<sup>6</sup>. Another numerical scheme calculates the sensitivity volume through a 3d integration grid consisting of lattice planes aligned parallel to the detector surface<sup>6,7</sup>. At each integration point the solid angle of detector is calculated including partial shadowing by the pinhole. with The most complete numerical approach would be to use Monte Carlo techniques to launch an ensemble of rays from the detector surface and trace them through to collisions with the as-built engineering model for detector aperture surfaces and the first wall. This process would result in a complete model

---

<sup>a)</sup>matthew.carr@ukaea.uk

<sup>b)</sup>See the author list of Meyer, H., et al. "Overview of progress in European medium sized tokamaks towards an integrated plasma-edge/wall solution." Nucl. Fusion (2017).

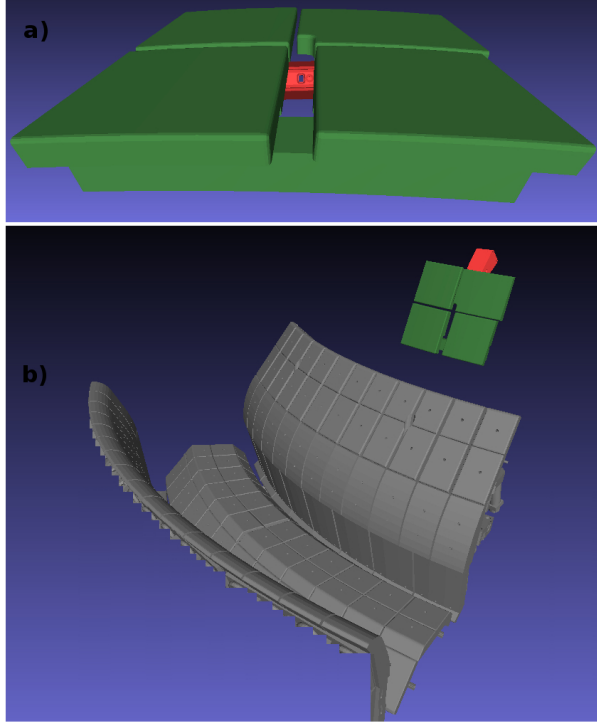


FIG. 1. a) Example visualisation of the FLH bolometer camera (red), which contains four bolometer foil sightlines, with its pinhole viewing between a first wall tile gap (green). In b) the same FLH camera is shown with its context viewing into the AUG divertor (grey). Note that the model detail has been reduced for visualisation.

of the coupling between the emission source and the detector including all 3D effects, such as occlusion and vignetting. Occlusion being when rays are obstructed by structures external to the camera (e.g. wall tiles), and vignetting being rays obstructed by the camera aperture. This Monte Carlo approach will be referred to as the volume ray-tracing technique.

The CHERAB code<sup>8,9</sup> was developed at JET as a platform for modelling spectroscopic diagnostics with the Raysect ray-tracing package<sup>10</sup>. Raysect is an open-source scientific ray-tracing framework that is capable of handling detailed 3D engineering geometry and physically accurate reflections. In this work CHERAB has been extended for use with bolometry by exploiting Raysect's Monte Carlo ray-tracing capabilities. The AUG bolometry system<sup>11</sup> was used as a case study diagnostic system for testing the relative benefits of the volume ray-tracing technique, although the conclusions should be generally applicable to other fusion devices.

## II. RAY TRACING BOLOMETER MODEL

The total power (radiant flux) measured by an observing surface is given by the integral of the incident emission over the collecting solid angle  $\Omega$  and surface area

A.

$$\Phi = \int_A \int_{\Omega} L_i(\mathbf{x}, \omega) \times \cos(\theta) d\omega dA \quad (1)$$

Here,  $L_i(\mathbf{x}, \omega)$  is the incident radiance arriving at a given point  $\mathbf{x}$  and incident angle  $\omega$  on the observing surface. The  $\cos(\theta)$  term is a geometry factor describing the increase in effective observing area as the incident rays become increasingly parallel to the surface.

Equation 1 is exact, but extremely difficult to evaluate analytically for any realistic bolometer foil geometry and radiation distribution. In practice, it is easier to evaluate this integral with Monte Carlo integration and importance sampling which approximates the integral with a weighted average<sup>12,13</sup>. The Monte Carlo integral estimator for a function  $f$  takes the form

$$I \approx \frac{1}{N} \sum_{j=1}^N \frac{f(x_j)}{p(x_j)}. \quad (2)$$

with  $f(x)$  evaluated at  $N$  sample points  $x_j$  and  $p(x_j)$ , given by

$$p(x_j) = \frac{q(x_j)}{\int q(x) dx}, \quad (3)$$

is the probability density function evaluated at the given sample point.  $q(x)$  is the weight function for cases when the sample points are drawn from a non-uniform sample distribution.

The lighting integral in equation 1 can be naturally discretised in terms of  $N_r$  rays, composed of 2D sample points  $\mathbf{x}_j$  on detector area  $A_d$  and sample vectors  $\omega_j$  on the hemisphere  $\Omega$ . Therefore, the estimator for the power arriving on a bolometer foil would take the form

$$\Phi \approx \frac{1}{N_r} \sum_{j=1}^{N_r} \frac{L_i(\mathbf{x}_j, \omega_j) \cos(\theta_j)}{p_A(\mathbf{x}_j) p_{\Omega}(\omega_j)}. \quad (4)$$

If the sample points are drawn uniformly over the detector area, then  $p_A(\mathbf{x}_j) = 1/A_d$ . The natural choice for sampling the vectors is a uniform hemisphere. However, for a bolometer detector the pinhole typically occupies a small solid angle leading to very computationally inefficient sampling. It is more efficient to sample the minimum cone of solid angle (with half angle  $\theta_h$ ) that tightly wraps the pinhole. If the vectors are generated uniformly over solid angle, the weighting function is still uniform,  $q(\omega) = 1$ , and thus the probability density function takes on the form of the fractional solid angle,  $p_{\Omega}(\omega_j) = 1/(2\pi(1 - \cos(\theta_h))) = 1/\Omega_{frac}$ . The estimator becomes

$$\Phi \approx \frac{\Omega_{frac} A_d}{N_r} \sum_{j=1}^{N_r} L_i(\mathbf{x}_j, \omega_j) \cos(\theta_j). \quad (5)$$

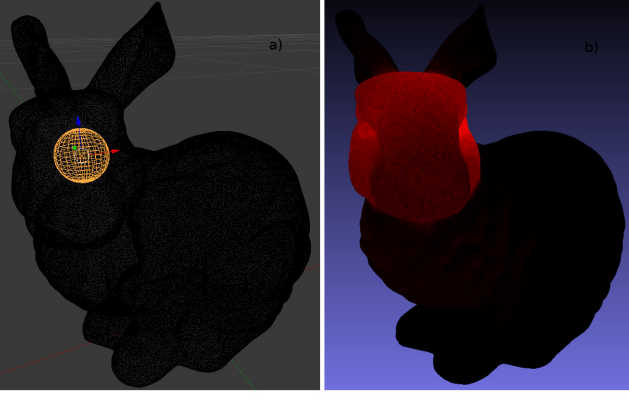


FIG. 2. a) The Stanford Bunny mesh with a spherical light-source of 1cm radius positioned in the head region. b) A log scaled power map of the power collected on the mesh surface elements.

### III. BENCHMARKING

To benchmark the implementation of equation 5, Raysect was configured to evaluate some test problems with a known analytic answer. All cases use a simple spherical volumetric source as the emitter but demonstrate the technique scales well to arbitrarily complex geometries.

Consider a sphere with a radius of 50cm centred at the origin. If the sphere has a uniform radiance of  $L_{sphere} = 1 \text{ W/m}^3/\text{str}$  then the total power radiated by the sphere's volume,  $V_{sphere}$ , is given by

$$\Phi_{theory} = L_{sphere} \times V_{sphere} \times 4\pi \approx 6.580 \text{ W}. \quad (6)$$

The radiating sphere can now be surrounded by an arbitrarily defined absorbing closed surface. As long as the surface does not intersect with the sphere, the total power collected by that surface through ray-tracing must equal the total power radiated,  $\Phi_{ray-tracing} = \Phi_{theory}$ . Changing the complexity of the confining surface provides a good benchmark since no matter how complex that surface becomes, the answer must always be the same.

Perhaps the simplest confining surface we can use is a cube centred on the origin with sides larger than the sphere's diameter. Note that due to symmetry we don't need to observe each face of the cube, only a single face multiplied by 6. Test case A consisted of a cube with a side length of 2 m, the results are tabulated along with the other cases in Table I.

Case B considers a circular detector surface of radius 5 mm at a distance of 2 m from the spherical source used in case A. The expected power measurement is given by total power radiated by the source multiplied by the fractional solid angle of the detector as seen by the source. This geometry approximates the scenario of a detector looking at a pinhole in the limit of large detector-pinhole separation.

Case	$N_r$	$\Phi_{theory} \text{ (W)}$	$\Phi_{ray-tracing} \text{ (W)}$	t (s)
A	$1 \times 10^6$	6.580	$6.551 \pm 0.057$	0.05
B	$1 \times 10^6$	$1.028 \times 10^{-5}$	$1.030 \pm 0.003 \times 10^{-5}$	0.08
C	$1 \times 10^7$	$5.264 \times 10^{-5}$	$5.282 \pm 0.037 \times 10^{-5}$	1.13

TABLE I. Benchmarking of the implementation of ray-tracing equation 5 with: case A a cube with a side length of 2 m; case B a pinhole camera like geometry with large detector pinhole separation; and case C the Stanford Bunny mesh surface<sup>14</sup>. The ray count and computation time are indicated for each case, along with the performance of the ray-tracing computation against the analytic result.

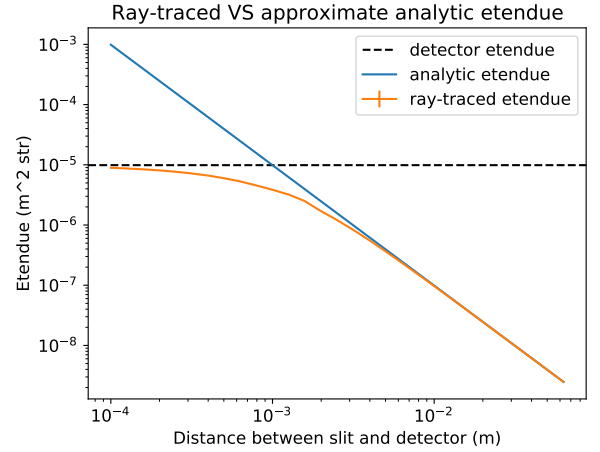


FIG. 3. The étendue of a simple pinhole camera composed of a circular detector and aperture with radius 1 mm as a function of detector-aperture separation. The ray-traced and analytical étendues are plotted against each other, along with the limiting detector étendue.

Case C used one of the most commonly used test models in computer graphics, the Stanford Bunny<sup>14</sup>. It is a collection of 69,451 triangles, and was assembled from a set of range scans of a clay bunny. The power load on each triangle in the mesh was individually ray-traced with equation 5, with the sum over the mesh triangles giving the total power absorbed by the surrounding surface. For this test, the volumetric source was 1 cm in radius and approximately centred in the bunny's head region, see Figure 2 for the source geometry.

All computations were performed on a 16 core Intel Xeon E5-2665 at 2.4 GHz.

### IV. ÉTENDUE CALCULATION

The étendue of the detector including occlusion and vignetting effects can be calculated by the weighted fraction of rays that pass through the slit multiplied by the full étendue that was sampled.

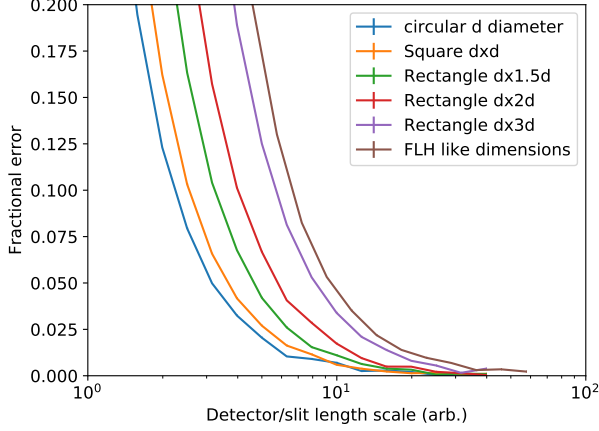


FIG. 4. The fractional error of the approximate analytical étendue relative to the ray-traced étendue for a number of different basic axis aligned aperture/detector geometries. The length scale is normalised to the smaller of the rectangular dimensions.

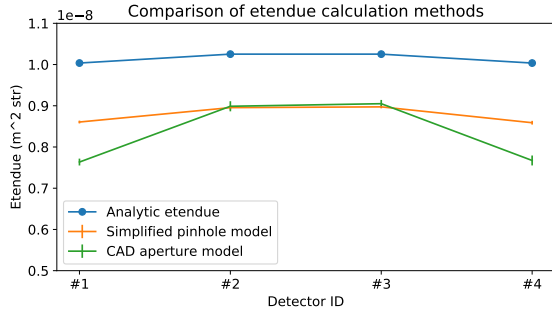


FIG. 5. The four foil detector étendues for the FLH camera were calculated with the analytic pinhole approximation (Eqn. 8) and these are compared with the ray-tracing étendue values (Eqn. 7). The three cases shown are a) the analytic pinhole approximation, b) the ray-tracing calculation with a realistic first wall model and a simplified pinhole in a rectangular plane, and c) as b) but also including the full as built detector geometry.

$$\epsilon_{det} = \frac{\Omega_{frac} A_d}{N_r} \sum_{j=1}^{N_r} \delta_j \cos(\theta_j), \quad \delta_j = \begin{cases} 0, & \text{ray hits} \\ 1, & \text{ray misses} \end{cases} \quad (7)$$

Here,  $\epsilon_{det}$  has units of  $[m^2 \text{ str}]$  and  $\delta_j = 0$  if the  $j$ th ray hits any of the obstructing aperture surfaces, or  $\delta_j = 1$  if the ray passes through unencombered to the plasma.

With this calculation the étendue for an arbitrary pinhole-foil geometry can be calculated to arbitrary precision with sufficient ray samples. By contrast, it is more common in bolometry to use the approximate pinhole formula<sup>2,4</sup>

$$\epsilon_{pin} = \frac{\cos(\gamma) \cos(\alpha) A_d A_p}{d^2}. \quad (8)$$

Where  $A_p$  is the rectangular pinhole area,  $d$  is the distance between the pinhole and detector, and  $\gamma, \alpha$  are compound angles describing the orientation of the foil surface with respect to the pinhole axis<sup>2,4</sup>.

The limiting behaviour of these two equations was explored with a simple pinhole geometry configuration. Consider a simple system where the detector and slit are both circular with a radius of  $r = 1$  mm. The detector and slit are on axis and separated by some variable distance of separation,  $d$ , that scans from 0.1 mm up to 10 cm. The plot in Figure 3 compares the ray-tracing results of equation 7 against the analytic approximation, equation 8.

As the separation tends to infinity the ray-tracing and analytic formula agree to within the numerical sampling noise. In the opposite limit the slit and detector eventually touch when the separation between them goes to zero. Since the detector and slit have the same geometrical shape and area, it is as if the slit was not present at all. And hence the étendue should tend towards the étendue of the detector on its own, represented by the dashed line in Figure 5. The ray-tracing result correctly tends to this limit while the analytic equation grows infinitely towards  $d = 0$ .

Figure 4 shows the relative error between the two calculation methods assuming the ray-tracing method is more accurate. The figure shows the impact of changing the axis aligned aperture/detector geometry from circular to square, and then increasingly elongated rectangles. The last data set includes an axis aligned aperture/detector combination with geometry similar to the installed FLH bolometer camera on AUG. Note that it is difficult to plot these curves on a normalised axis because of the subtle geometry differences between the different shapes. However, it demonstrates that the circular aperture is the limiting case and elongating the geometry leads to more deviation. Detectors and apertures are often elongated in the toroidal direction in fusion tomography systems to improve the signal to noise without significantly affecting the feature resolution.

The difference between the two étendue calculation methods was calculated for all AUG bolometer cameras. An extreme example case is shown for the FLH camera in Figure 5. The ray-tracing calculation was done with both b) a simplified and c) full detail aperture to separate out the different contributions. The simplified aperture used a rectangular plane with a rectangular pinhole cut out of the plane, whereas c) used the full detail engineering model of the as built detector.

There is a systematic offset between the analytic a) and ray-traced simple pinhole b) cases of order  $\sim 10\%$ , which is due to performing the calculation with a simplified geometry. The extra drop in étendue between b) and c) is due to vignetting effects at the edges of the camera field of view when the full CAD geometry is included.

The étendue calculations for the FHC camera had an average deviation of 10.8% compared with the much smaller 2.7% on the FLX camera. It was found that

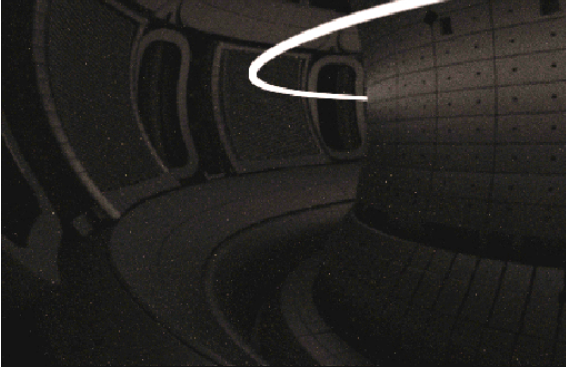


FIG. 6. A 3D voxel basis function composed of a toroidally symmetric annulus with uniform emissivity. The full engineering model for the first wall is included in all ray-tracing calculations. Reflection effects have been turned on for visualisation purposes.

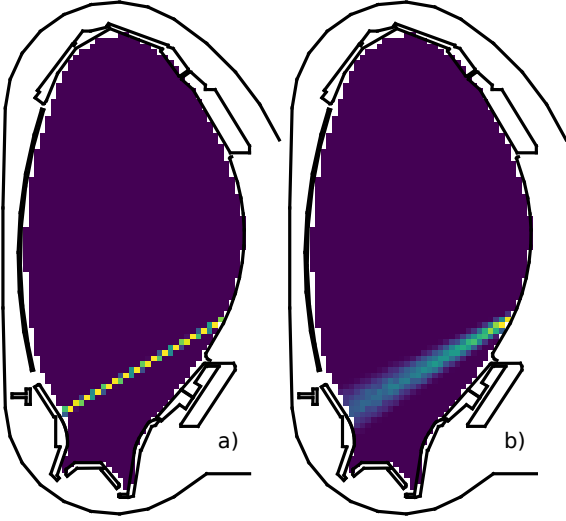


FIG. 7. Comparison of sensitivity matrices  $\mathbf{W}$  in the poloidal plane for a bolometer foil modelled with a single-ray and a volume sampled light cone.

each camera had a distinctly different mean deviation, which is likely due to differences in the camera geometry that have more or less effect on the assumptions in 8. These étendue deviations act as an extra systematic noise source in the inversion process.

## V. SENSITIVITY MATRICES

Recovering the plasma emission with tomography is an ill-posed problem. It is customary to describe the system in terms of a sensitivity matrix  $\mathbf{W}$ . The elements  $W_{k,l}$  describe the coupling between the  $N_s$  plasma emission sources  $x_l$  and measured power  $\Phi_k$  at  $N_d$  detectors. The whole detector set is typically represented as the matrix

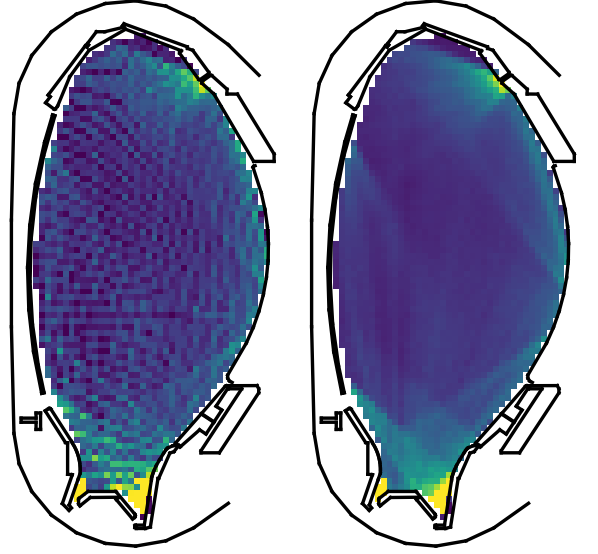


FIG. 8. Comparison of the sight line densities for foil bolometers at AUG modelled with single-ray paths and volume sampled light cones.

equation

$$\Phi = \mathbf{W}\mathbf{x}. \quad (9)$$

The power for the  $k$ th detector can be expressed as

$$\Phi_k = \sum_{l=1}^{N_s} W_{k,l} x_l, \quad (10)$$

where  $k$  and  $l$  are the indices for the detectors and sources respectively. There are a number of possible choices for the prescription of the emitting source  $l$  basis functions<sup>15</sup>. In this work we have used a 3d voxel composed of a toroidally symmetric annulus with uniform emissivity  $x_l$ , see Figure 6 for a visualisation of a single voxel element. Equation 9 can then be inverted using established tomography techniques<sup>2,3</sup> to yield the spatial emissivities from a measured set of power values.

The conventional analysis technique estimates the single ray sensitivity matrix  $\mathbf{W}_{\text{SR}}$  by tracing a straight line through the system, originating at the centre of the detector surface and passing through the slit centre. Every sensitivity element  $W_{k,l}$  is weighted by the length of the ray segment,  $s_{k,l}$ , that intersects with the  $l$ th emitting source approximated as a 2d cell.

$$\mathbf{W}_{\text{SR}} : W_{k,l} = s_{k,l} \times \epsilon_{\text{pin}} \quad (11)$$

In contrast, the ray-tracing technique launches  $N_r$  randomly generated rays from the detector and performs a weighted sum of the ray lengths,  $s_{j,k,l}$ , that intercept with the 3d voxel using equation 5. Rays that collide with the slit geometry or miss the cell have a zero weighting.

$$\mathbf{W}_{\text{Vol}} : W_{k,l} = \frac{\Omega_{\text{frac}} A_d}{N_r} \sum_{j=1}^{N_r} s_{j,k,l} \cos(\theta_j) \quad (12)$$



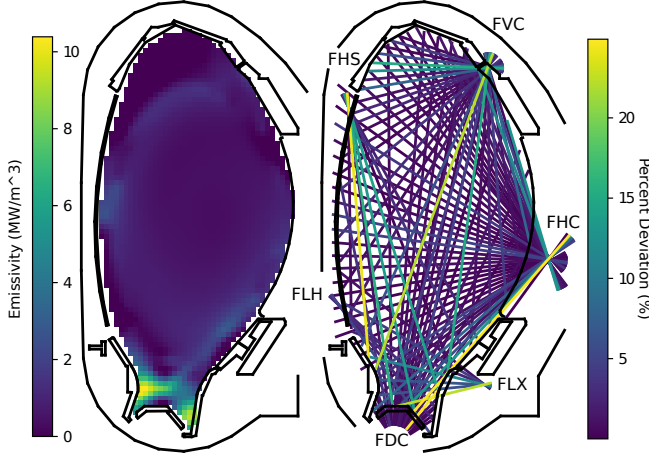


FIG. 9. Figure a) shows the BLB code inverted emission profile for AUG shot 33280 at 4.1s. Figure b) shows the forward calculated sightlines colour-coded by the percentage error between the two techniques. The bolometer camera positions are labeled.

Sensitivity matrices for all AUG bolometer cameras were calculated with a 2206 cell inversion grid, taking between 1 - 4 hours per camera on a 16 core Intel Xeon E5-2665 at 2.4 GHz.

Fig. 7 compares the sensitivity matrices for a single detector generated with the single ray and the volume ray-tracing methods. The single ray method exhibits spatial aliasing since neighbouring cells along the ray path can be weighted by a corner intersection and then a longer intersection, leading to a repeating cell pattern. On the other hand, the volume sampling method leads to a smoother spatial response and the sensitivity region correctly expands as you get further from the detector. Also, the toroidal bending of the voxels is automatically included due to the 3D nature of the calculation method.

A clear advantage of the volume sampling method is that the weight matrices are less sensitive to design tolerances. Small changes in the position and direction of a single sightline can produce quite a big difference in the aliasing pattern of the weight matrix. On the other hand, the volume ray-tracing matrix is much more stable to small perturbations in the input parameters.

Fig. 8 compares the sight line density for the whole AUG foil bolometer detector set calculated with the two methods. The sightline density matrix is the normalised sum over the  $k$  index in  $\mathbf{W}$ , yielding a relative measure of how well a source region  $l$  is observed relative to the other cells. For the single ray technique there are a number of cells in the plasma emission region that are effectively dark, i.e. not seen at all by a detector in the model. These cells can only be filled in by regularisation.

To study these effects further we have used an example radiation scenario from AUG shot 33280 at 4.1s inverted with the currently applied AUG tomography code<sup>16</sup>, shown in Fig. 9 a). This tomography code uses

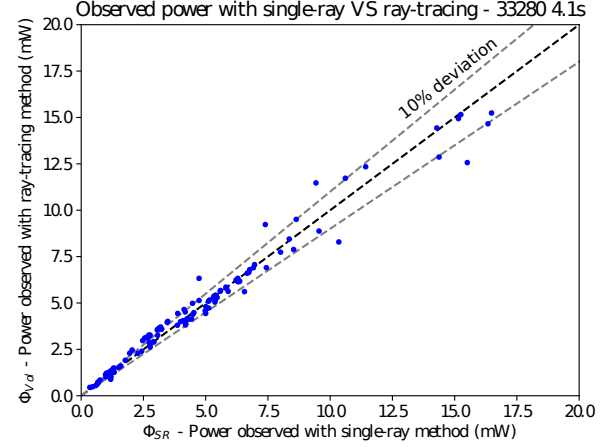


FIG. 10. Plot of the forward modelled power with the single-ray technique,  $\Phi_{SR}$ , against the power calculated with ray-traced volumes,  $\Phi_{Vol}$ , for each detector observing the radiation scenario in Figure 9. The deviations become more pronounced at higher powers which tends to correlate with sightlines that see the divertor.

the conventional single ray model for its inversions. Fig. 9 b) shows each sightline colour coded by the percentage error in the observed power when the single-ray approximation is used in comparison to volume ray-tracing. Similarly, Fig. 10 shows a scatter plot of the forward modelled power calculated with a single-ray,  $\Phi_{SR}$ , against the power calculated with a ray-traced volume,  $\Phi_{Vol}$ , for each detector.

For many detectors observing lower powers the single sight line is a good approximation, these sightlines are looking across the bulk plasma which is characterised by smoother emission gradients. However the errors can become more significant ( $> 10\%$ ) for sightlines that see the divertor region with strong gradients, such as strike point and x-point radiation. Single ray sightlines that tend to see a locally bright source will over-estimate the power, whereas sightlines that narrowly miss a bright source (such as a strike point) will under-estimate the power. It is also possible to under-estimate the power due to occlusion effects where the single ray path terminates too early compared to the full collection volume. An example of a sightline with this characteristic is shown in Fig. 11.

## VI. PERFORMANCE VS PHANTOMS

To explore the differences between reconstruction results obtained using the two sensitivity matrices, the two methods were tested on a standard population of 94 phantom emission scenarios<sup>17</sup> used to benchmark the existing tomography code<sup>16</sup>. The 94 phantoms form a standard set of test cases constructed from combinations of six basic emission sources: uniform backgrounds with



FIG. 11. Example case where the single-ray path terminates too early on a tile surface. When the volume ray-tracing technique is used a large fraction of the collection volume extends into the inner divertor resulting in a significant error in the collected power calculation.

	Phantom	SR	VOL	SR + Reg	VOL + Reg
	a)	b)	c)	d)	e)
$P_{rad}$ (MW)	13.82	13.37	13.76	13.45	13.7
$\rho_c$		0.68	0.85	0.79	0.89

TABLE II. The total radiated power,  $P_{rad}$ , and Pearson correlation coefficient,  $\rho_c$ , for each of the inversions in Figure 12. The regularised inversions have  $\beta_L = 0.0125$ .

gradients; point sources; x-points; strike points; divertor legs; and radiation rings on a flux surface<sup>17</sup>. The full population of phantoms are designed to test the systems ability to resolve representative emission features that may be encountered in real plasmas.

Virtual observations for each phantom are constructed by multiplication of the volume sensitivity matrix with the phantom's emissivity vector, as per equation 9. In addition, 5% gaussian distributed noise was added to the virtual observations to simulate all uncertainties such as systematic errors in the detector alignment and calibration, as well as instrument noise in the detector electronics.

There are a wide range of inversion schemes used in fusion tomography diagnostics<sup>2</sup>, perhaps the most widely used is the Phillips-Tikhonov regularisation scheme combined with an anisotropic diffusion model as the objective function<sup>16</sup>. In this work the population of phantoms was inverted with the Simultaneous Algebraic Reconstruction Technique (SART)<sup>18</sup>. Using an iterative inversion scheme like SART allows the inversion method to have a minimum amount of prior information. The strength of the smoothness hyper-parameter,  $\beta_L$ , could be scanned in order to quantify how far the results are independent of prior information. In addition, iterative schemes provide an easy way to enforce positivity, since every iteration the cells with negative emissivity can be clamped to zero. For more details on the SART implementation and regularisation parameters chosen see the appendix.

To measure the performance of the inversions we have opted for the Pearson correlation coefficient,  $\rho_c$ , which can measure the correlation between two vectors<sup>21</sup>. In this context it is defined as the covariance of the two emis-

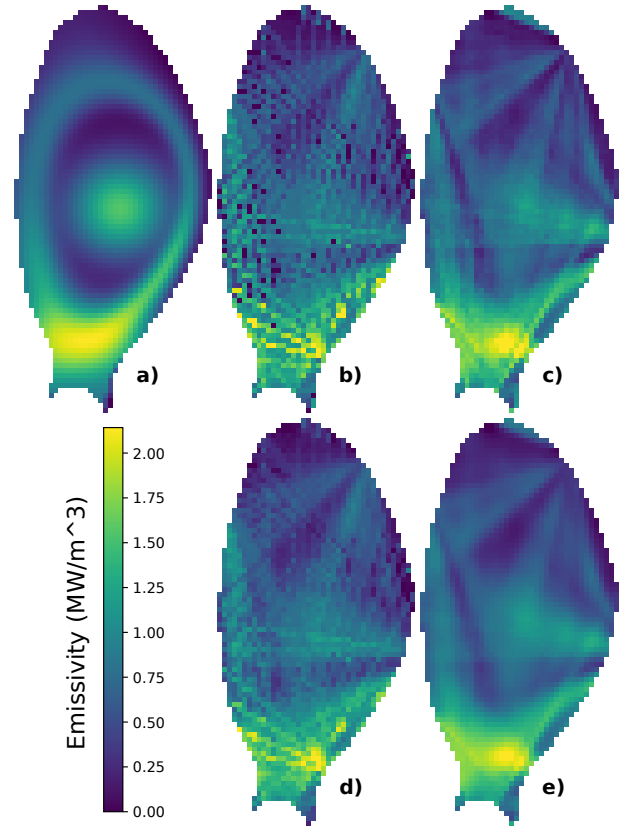


FIG. 12. Bolometer foil measurements of the phantom emission scenario given in a) have been forward modelled with the volume ray-tracing method. The synthetic measurements are then inverted with the unregularised SART algorithm using weight matrices constructed with the single-ray approximation b) and the volume ray-tracing method c). The differences between b) and c) demonstrate the extra spatial constraints imposed by volume ray-tracing. Additionally, both single-ray and ray-tracing inversions were used with regularised SART in d) and e) respectively. See Table II for a comparison of the results.

sion source vectors, inversion  $\mathbf{x}_{inv}$  and phantom solution  $\mathbf{x}_{sol}$ , divided by the product of their standard deviations,

$$\rho_c = \frac{\text{Cov}(\mathbf{x}_{inv}, \mathbf{x}_{sol})}{\sigma(\mathbf{x}_{inv})\sigma(\mathbf{x}_{sol})}. \quad (13)$$

The SART inversions were performed on all 94 phantoms with weight matrices computed with both the single-ray ( $\mathbf{W}_{SR}$ ) and volume ray-tracing ( $\mathbf{W}_{VOL}$ ) techniques, both with and without the Laplacian gradient regularisation. The resulting inversions for an example phantom are shown in Figure 12, with an accompanying comparison of the total radiated powers and correlation coefficients to the phantom in Table II. The differences between Fig. 12 b) and c) demonstrate the extra spatial constraints imposed by the volume ray-tracing method. The  $\mathbf{W}_{VOL}$  matrix continues to outperform  $\mathbf{W}_{SR}$  for the same level of gradient regularisation.

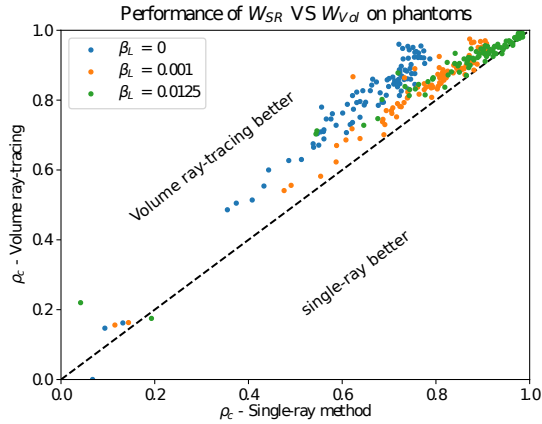


FIG. 13. Performance on all 94 phantoms of the two weight matrices,  $\mathbf{W}_{\text{SR}}$  and  $\mathbf{W}_{\text{Vol}}$  for varying levels of regularisation. The performance measure is the Pearson correlation coefficient, where  $\rho_c = 1$  means the inverted emission profile is identical to the phantom emission profile.

Figure 13 shows the performance on all phantoms for varying levels of regularisation. It demonstrates that the volume ray-tracing matrices are naturally more spatially constrained and require lower levels of regularisation for the same performance with single-rays. Furthermore, it is clear from Fig. 13 that turning up the regularisation is mainly affecting the single ray inversions. At higher levels of regularisation, the two distributions are in more agreement because regularisation is a property of the solution matrix, not the sensitivity matrix, and hence regularisation can dominate the solution. However, even at the highest regularisation level there is still a clear offset demonstrating the volume ray-tracing technique has superior performance.

Figure 14 shows the distribution of total radiated power for each inversion plotted against the phantom's real total radiated power. The distributions are plotted for both the single-ray and volume ray-tracing techniques using the middle regularisation case. The spread of points for the  $\mathbf{W}_{\text{SR}}$  case is bigger than the  $\mathbf{W}_{\text{Vol}}$  distribution with mean deviations of  $5.2 \pm 4.1\%$  and  $1.7 \pm 1.5\%$  respectively.

## VII. DISCUSSION

The volume ray-tracing technique is expected to have the most impact on fusion machines where the solid angle of the detectors is sufficiently large that the beam width of the detector sensitivity spans multiple plasma features or gradients. Therefore this technique could have an impact on highly radiating divertor scenarios where the bulk of the radiation is local to the divertor and significant radiation gradients may be present<sup>1</sup>. The impact will be much less when the detector's sensitivity is highly collimated compared to the inversion grid.

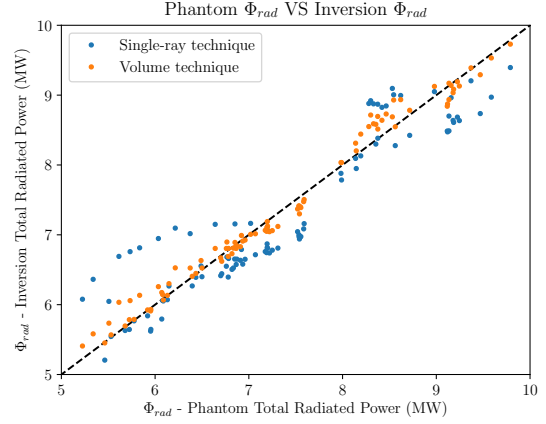


FIG. 14. The phantoms' total radiated power,  $\Phi_{\text{rad}}$ , plotted against the inverted solution  $\Phi_{\text{rad}}$  for all 94 phantoms using the single ray and volume ray-tracing techniques. Inversion performance decreases as the inversion points move away from the dashed line. This dataset used the middle regularisation case ( $\beta_L = 0.001$ ) and demonstrates the volume-raytracing technique consistently out performs the single ray model.

The volume ray-tracing approach tends to produce weight matrices where every grid cell is seen by multiple detectors. This has a natural smoothing effect on the solution matrix. The AUG bolometry system has a very high degree of spatial coverage and only  $\sim 5\%$  dark cells in the inversion grid. But these effects can be more significant on other machines with poorer spatial coverage. Studies of the JET bolometry system came to similar conclusions and found it was necessary to include the full geometry effects rather than relying on the line-integral approximation<sup>4</sup>.

Regularisation normally smooths over many sources of error in an inversion process. Using volume ray-tracing to calculate the étendue and sensitivity matrices allows us to use a more physical model of the detector response, and hence helps remove some of the systematic error sources. Therefore it is not surprising that the volume ray-tracing approach has better performance at a given level of regularisation.

However there are still other errors, such as detector noise and design errors that are always present in the data. There are also physical effects such as energy deposition/reflection of neutral particles and the finite foil reflectivity as a function of wavelength. The improvement due to volume ray-tracing degrades with increasing levels of noise, where higher levels of regularisation are required. So it is important to have a system with a high level of signal to noise to see the benefits from this technique. On the other hand, there does not appear to be any disadvantages from including the extra calculation detail in the inversions.

The calculations for volume ray-tracing are more computationally intensive than for a single ray, however they only need to be calculated once. Re-calculation is only



required when changing the inversion grid or the detectors, which is typically between experimental campaigns.

The volume ray-tracing method can be used with combined pinhole camera and machine first wall geometry to accurately model complicated compound apertures. This technique opens up a new design space for bolometer configurations that might not normally be considered, potentially helping to expand the tomography coverage in machines with poor accessibility.

## VIII. CONCLUSIONS

Volume ray-tracing techniques combined with full 3D machine models have been used to calculate the étendue and sensitivity matrices of the bolometry system at ASDEX-Upgrade. The volume ray-traced sensitivity matrices were benchmarked against sensitivity matrices calculated with the more conventional single-ray technique. The volume ray-tracing technique can include vignetting and occlusion effects from installation features that are not possible to include in simpler calculation methods.

Inversions using both matrices were carried out on a population of emission phantoms with varying levels of regularisation. The volume ray-tracing technique consistently out-performed the single-ray technique in regards to both the correlation coefficient distance measure and the accuracy of the inverted total radiation power. The volume ray-tracing technique was shown to be naturally more spatially constrained.

The technique is a useful addition to the standard bolometry techniques currently in use and doesn't present any obvious disadvantages. However, the volume ray-tracing method requires detailed in-situ information of the system and the improvements gained from including the extra geometric detail degrade quickly with increasing sources of error such as detector noise and design errors. It is important for a bolometry system to have good signal to noise ( $\leq 5\%$  detector noise) to gain significant benefit from the extra calculation detail.

## ACKNOWLEDGMENTS

The authors wish to acknowledge the contributions of V. Brack at IPP Garching who extracted the relevant bolometer camera geometry from the engineering CAD files.

This work has been carried out within the framework of the EUROfusion Consortium and has received funding from the Euratom research and training programme 2014-2018 under grant agreement No 633053 and from the RCUK Energy Programme [grant number EP/P012450/1]. The views and opinions expressed herein do not necessarily reflect those of the European Commission.

B. Lipschultz was funded in part by the Wolfson Foundation and UK Royal Society through a Royal Society

Wolfson Research Merit Award as well as by the RCUK Energy Programme (EPSRC grant number EP/I501045).

## Appendix: Tomographic inversion method

The population of phantoms were inverted with the Simultaneous Algebraic Reconstruction Technique (SART)<sup>18</sup>. The SART method is an iterative inversion scheme where the emission cells are updated with the formula

$$x_l^{(i+1)} = f_{sart}(x_l^{(i)}) = x_l^{(i)} + \frac{\omega}{W_{\oplus,l}} \sum_{k=1}^{N_d} \frac{W_{k,l}}{W_{k,\oplus}} (\Phi_k - \hat{\Phi}_k), \quad (\text{A.1})$$

where

$$W_{k,\oplus} = \sum_{l=1}^{N_s} W_{k,l}, \quad W_{\oplus,l} = \sum_{k=1}^{N_d} W_{k,l}.$$

Here  $x_l^{(i)}$  is the previous estimate for the emission at source  $l$  in iteration  $i$ . The relaxation hyperparameter was set to  $\omega = 1$  for this study. The SART method effectively updates each cell by the weighted average error between the forward modelled  $\hat{\Phi}_k$  and observed  $\Phi_k$  measurements. The observed errors are weighted by both their proportion of the total ray length ( $W_{k,\oplus}$ ) and the sum of the effective ray paths crossing that cell ( $W_{\oplus,l}$ ).

Because the inversion process is an ill-posed problem, there are technically an infinite sea of solutions to equation 9. The sensitivity matrix  $\mathbf{W}$  can have a non-trivial null space, meaning that any linear combination of null space models can be added to a particular solution and not change the fit to the data. Regularisation is a technique that applies additional constraints in the form of an objective function to bias the inversion process towards solutions that satisfy our prior knowledge<sup>2,20</sup>. The objective function is a regularisation operator that quantifies some property of the emission profile such as Laplacian smoothness, anisotropic smoothness or minimum cross-entropy.

The current AUG code employs the Anisotropic Diffusion Model Tomography<sup>16</sup> (ADMT) scheme, which assumes that radiation varies less along magnetic flux surfaces than perpendicular to them. This scheme uses an anisotropic smoothness operator and is prescribed in terms of two diffusion terms, perpendicular  $D_{\perp}$  and parallel  $D_{\parallel}$  to flux surfaces. In this work we have opted for an isotropic 2D discrete Laplacian smoothness operator<sup>19</sup>,

$$\hat{\mathcal{L}}_{iso}(x_l^{(i)}) = \beta_L (C x_l^{(i)} - \sum_{c=1}^C x_c^{(i)}). \quad (\text{A.2})$$

Here,  $c$  is the index for the sum over the eight possible neighbouring cells. See Figure 15 for an example of the operator in two different grid positions. With the Laplacian smoothness objective the update formula becomes

$$x_l^{(i+1)} = f_{sart}(x_l^{(i)}) - \hat{\mathcal{L}}_{iso}(x_l^{(i)}). \quad (\text{A.3})$$

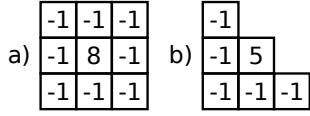


FIG. 15. Examples of the 2D Laplacian operator for a) a central cell ( $C = 8$ ) and b) a cell near the inversion grid corner ( $C = 5$ ).

There are two regularisation hyperparameters in this scheme. The first is  $\beta_L$  which determines the amount of local smoothness imposed. When  $\beta_L = 0$ , the solution is fully determined by the measurements, and as  $\beta_L \rightarrow 1$ , the solution is dominated by the smoothness operator. The criterion for choosing the value of  $\beta_L$  can be determined by a constraint such as the misfit between the forward modelled  $\hat{\Phi}_k$  and observed  $\Phi_k$  measurements, or the L-curve method<sup>20,22</sup>. In this work the  $\beta_L$  parameter was scanned in order to quantify how far the results are independent of prior information.

The other regularisation parameter is the criterion for terminating the SART iterations. In the implemented scheme the iteration loop was broken when either the difference between successive  $\chi^2$  values fell below  $10^{-4}$ , or a maximum of 250 iterations was reached.

After every iteration, all cells with negative emissivity were clamped to zero to enforce positivity.

In future work the isotropic smoothness operator could be exchanged for two 2D discrete gradient operators aligned parallel and perpendicular to the local magnetic field,  $\hat{\mathcal{L}}_{\parallel}$  and  $\hat{\mathcal{L}}_{\perp}$ , with accompanying hyperparameters  $\beta_{\parallel}$  and  $\beta_{\perp}$ . These anisotropic operators would have an effect similar to the established ADMT scheme<sup>16</sup> and allow further assessment of the value of including the extra geometric detail when known physics is present.

<sup>1</sup>F. Reimold, et al. Nucl. Fusion 55, 033004 (2015).

<sup>2</sup>L. C. Ingesson, et al. Fusion Technology 53, 528 (2008).

<sup>3</sup>T. Craciunescu, et al. Nucl. Instrum. Methods Phys. Res. Sect. A 605, 374 (2009).

<sup>4</sup>L. C. Ingesson, C. F. Maggi and R. Reichle, Rev. Sci. Instrum. 71, 1370 (2000).

<sup>5</sup>L. C. Ingesson, P. J. Böcker, R. Reichle, M. Romanelli and P. Smeulders, J. Opt. Soc. Am. A 16, 17 (1999).

<sup>6</sup>M. Weiland, et al. Plasma Phys. Control. Fusion 57, 085002 (2015).

<sup>7</sup>D. Vezinet, et al. Nuclear Fusion 56, 086001 (2016).

<sup>8</sup>C. Giroud, et al. “CHERAB Spectroscopy Modelling Framework (Version v0.1.0)”. Zenodo. <http://doi.org/10.5281/zenodo.1206142>, (2018).

<sup>9</sup>M. Carr et al 2017 “Towards integrated data analysis of divertor diagnostics with ray-tracing”. 44th EPS Conf. on Plasma Physics (Belfast, Northern Ireland UK, 2630 June 2017) (<http://ocs.ciemat.es/EPS2017PAP>).

<sup>10</sup>A. Meakins and M. Carr, “Raysect Python Raytracing Package (Version v0.4.0)”. Zenodo. <http://doi.org/10.5281/zenodo.1205064>, (2017).

<sup>11</sup>M. Bernert, et al. Rev. Sci. Instrum. 53, 104003 (2014).

<sup>12</sup>M. Pharr, and G. Humphreys, “Physically based rendering: From theory to implementation”. Morgan Kaufmann, (2016).

<sup>13</sup>E. Veach, “Robust Monte Carlo methods for lighting simulation”. PhD thesis, Stanford University, (1997).

<sup>14</sup>G. Turk, and M. Levoy. “Zippered polygon meshes from range images.” Proceedings of the 21st annual conference on Computer graphics and interactive techniques. ACM, 1994.

<sup>15</sup>L. C. Ingesson, H. Chen, P. Helander and M. J. Mantsinen, Plasma Phys. Control. Fusion 42, 161 (2000).

<sup>16</sup>J. C. Fuchs, et al. Europhysics Conference Abstracts: 21st Conf. Controlled Fusion and Plasma Physics, Montpellier, June 27, 18B, 1308 (1994).

<sup>17</sup>S. Glöggler, “Development of an Algorithm to Determine the Total Radiated Power (IPP 2018-06)”. Garching: Max-Planck-Institut für Plasmaphysik. doi:10.17617/2.2564760, (2018).

<sup>18</sup>A. Andersen, and A. Kak, Ultrasonic imaging 6, 81 (1984).

<sup>19</sup>T. Hobiger, T. Kondo, and Y. Koyama, Earth, planets and space, 60, 727 (2008).

<sup>20</sup>R. Aster, B. Borchers, and C. Thurber, “Parameter estimation and inverse problems”. Vol. 90. Academic Press, (2011).

<sup>21</sup>K. Pearson, Proc. R. Soc. 58, 240 (1895).

<sup>22</sup>P. C. Hansen, SIAM Review 34, 561 (1992).